GPU simulation of wake effects at the Horns Rev 1 offshore wind farm using the CFD porous disk wake model

Uchida, Takanori
Research Institute for Applied Mechanics (RIAM), Kyushu University

Tanaka, Teppei
Eurus Energy Holdings Corporation

Shizui, Ryuta
Eurus Energy Holdings Corporation

Ichikawa, Hiroto
Eurus Energy Holdings Corporation

他

出版情報：Wind Engineering. 47 (2), pp.408-421, 2023-04. SAGE Publications
バージョン：

GPU Simulation of Wake Effects at the Horns Rev 1 Offshore Wind Farm using the CFD Porous Disk Wake Model

Takanori Uchida*
Research Institute for Applied Mechanics (RIAM), Kyushu University, 6-1 Kasuga-kouen, Kasuga, Fukuoka 816-8580, Japan
* Corresponding Author: takanori@riam.kyushu-u.ac.jp; Tel.: +81-92-583-7776; Fax: +81-92-583-7779.

Teppei Tanaka, Ryuta Shizui, Hiroto Ichikawa, Ryo Takayama, Kazuomi Yahagi, Ryoya Okubo
Eurus Energy Holdings Corporation, Hulic Kamiyacho Building 7F, 3-13, Toranomon 4-chome, Minato-ku, Tokyo, 105-0001, Japan
teppei.tanaka@eurus-energy.com
ryuta.shizui@eurus-energy.com
hiroto.ichikawa@eurus-energy.com
ryo.takayama@eurus-energy.com
kazuomi.yahagi@eurus-energy.com
ryoya.okubo@eurus-energy.com

Abstract: To verify the effectiveness of the GPU simulation of wake effects at a large-scale offshore wind farm, we ran an in-house large-eddy simulation (LES) solver with a CFD porous disk wake model for the Horns Rev 1 wind farm. For this numerical research, we prepared the latest workstation equipped with a Xeon W-2265 CPU and an NVIDIA RTX A6000 GPU. We clarified that the calculation speed of the single GPU of the NVIDIA RTX A6000 is approximately 10 times faster than the calculation speed of the Xeon W-2265. Careful data analysis and visualization of the unsteady turbulent flow fields obtained in the current LES study suggest that the mutual interference of the wakes developed by wind turbines may frequently form a local speed-up region around wind turbines, located on the downstream side of large offshore wind farms.

1. Introduction

The Government of Japan is aiming for the "realization of a carbon-free society in 2050," and offshore wind power generation is particularly key to achieving this goal. As a wind turbine blade rotates, a wind speed deficit region called the wind turbine wake is formed on the downstream side of the wind turbine (Porté-Agel et al., 2020). In a large offshore wind farm consisting of multiple wind turbines, wind turbine wakes can interfere with one another. The downstream wind turbines are directly affected by this, leading to decreased power generation and an increased wind load (Hasager et al., 2013).

Figure 1 provides an aerial view of wake clouds at the Horns Rev 2 offshore wind farm in Denmark, as published by Hasager et al. (2013). The Horns Rev 2 offshore wind farm is located in the North Sea, west of Jutland, Denmark. The wind farm consists of 91 wind turbines with a hub-height 68 m above the mean sea level. Horns Rev 2 entered full operation in November 2009. The wind turbine wakes are visualized by low-hanging fog that mixes into the wake region. When observing the aerial view shown in Figure 1 in detail, the mutual interference phenomenon of the wind turbine wakes, as described above, can be clearly observed.

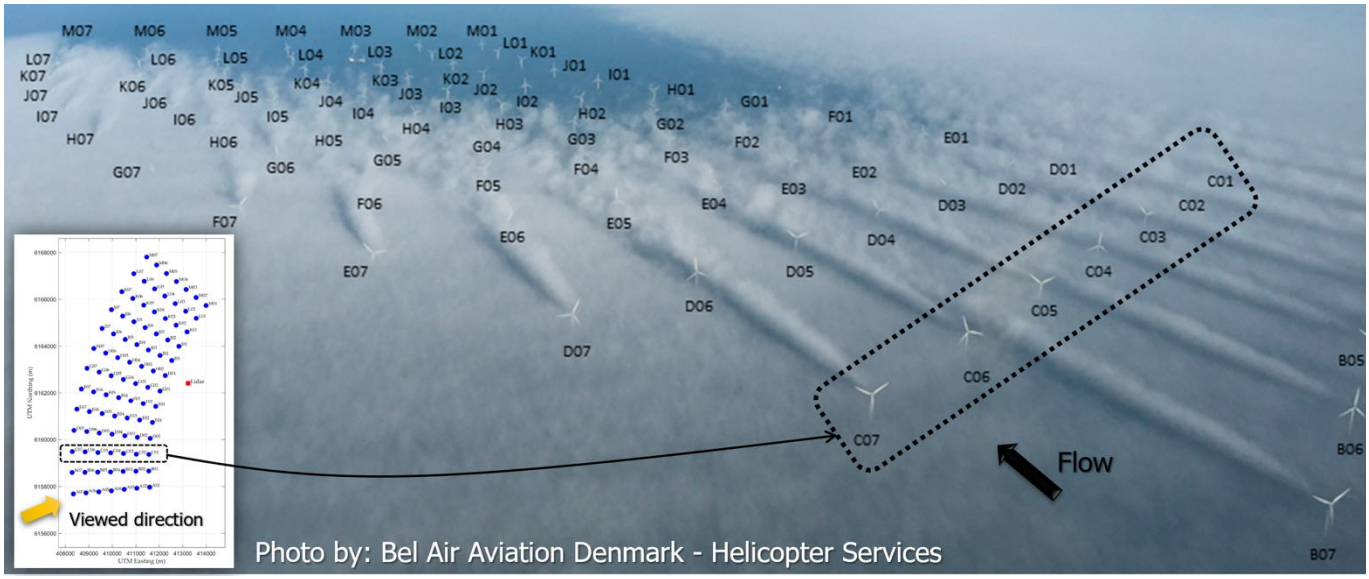

Figure 1. Photograph of the Horns Rev 2 offshore wind farm on 25 January 2016 at 12:45 UTC, seen from WSW (Hasager et al., 2013). The Horns Rev 2 offshore wind farm is located in the North Sea, west of Jutland, Denmark.

To better construct a large offshore wind farm in Japan, there is an urgent need to develop a wake model that can accurately predict the mutual interference phenomenon of wind turbine wakes. In response to these social and engineering demands, the first author of the current paper is developing a CFD porous disk wake model by better evaluating the bankability and aiming for efficient cost reduction (Uchida et al., 2020, 2021). To verify the prediction accuracy of the CFD porous disk wake model, Uchida et al. (2020) conducted wind tunnel experiments and numerical simulations to determine the utility-scale of the model. In the numerical simulation, fully resolved geometries were developed and combined with CFD, and an average wind speed database for wind turbine wakes was created. Based on the wind speed database described above, the researchers verified the predicted accuracy of the CFD porous disk wake

model. The model was able to reproduce the wind speed database with an error rate of 10% or less in the wake region of 5–10 D (D is the diameter of the wind turbine). Uchida et al. (2021) organized supervisory control and data acquisition (SCADA) data for a utility-scale wind turbine and measured the flow field of the wind turbine wake using the latest vertical profiling Lidar measuring device. The researchers quantitatively demonstrated that the current wake model could reproduce the 10-minute average wind speed with an error rate of 10% or less.

In parallel with the development and verification of the above CFD porous disk wake model, it is also extremely important that we significantly reduce the simulation time of the in-house LES solver implemented in the current wake model (Gargallo-Peiró et al., 2018; Ono et al., 2019). Therefore, in the current paper, we examine a GPU simulation of wake effects for the Horns Rev 1 offshore wind farm using the CFD porous disk wake model. The Horns Rev 1 offshore wind farm is located approximately 20 km southeast of the Horns Rev 2 offshore wind farm.

2. Numerical Set-Up

For our numerical technique, the finite-difference method (FDM), based on a Cartesian grid system, was adopted and large-eddy simulation (LES) was used for the turbulence model. For the governing equations of flow in the tensor form (i, j = 1, 2, 3), a filtered continuity equation for incompressible fluid (Equation (1)) and a filtered Navier–Stokes equation (Equation (2)) were used. For the computational algorithm, the fractional step (FS) method (Kim et al., 1985) was used, and a time-marching approach based on the simplest explicit and one-step method was adopted. Poisson's equation for pressure was solved using the successive over-relaxation (SOR) method. For the discretization of all spatial terms, except for the convective term in Equation (2), a second-order central difference scheme was applied. For the convective term, a third-order upwind difference scheme was employed. The interpolation technique (Kajishima, 1994) was used for the fourth-order central differencing that appears in the discretized form of the convective term. For the weighting of the numerical diffusion term in the convective term discretized by third-order upwind differencing, α = 0.5 was used, as opposed to α = 3.0 from the Kawamura–Kuwahara scheme (Kawamura et al., 1986), to minimize the influence of numerical diffusion. For LES subgrid-scale modeling, the explicit mixed timescale (MTS) model (Inagaki et al., 2005) based on an eddy viscosity assumption was adopted (Equations (3)–(11)) for the turbulent flow field, and Simpson's rule was used as the test filter in the MTS procedure. For the rotation of the wind turbine blades, the CFD porous disk wake model was utilized (Uchida et al., 2020, 2021). The effect of the CFD porous disk wake model, described in Equations (12) and (13), was implemented as an external force in Equation (2). The only parameter of the CFD porous disk wake model, C_{RC}, was the resistance coefficient. We conducted a thorough preliminary investigation of the resistance coefficient (C_{RC} = 1.0–10 in 0.5 increments), based on which we adopted 5.0 for the coefficient (C_{RC}) (Equation (14)), with a cosine-shaped distribution function in the swept area, as was shown in previous papers (Uchida et al., 2020, 2021). In previous work, the in-house LES solver and Reynolds-averaged Navier–Stokes (RANS)-based commercial CFD software were compared, and it was shown that the in-house LES solver provided comparable results to those of the RANS-based commercial software (Uchida et al., 2018).

$$\frac{\partial \overline{u}_i}{\partial x_i} = 0$$	(1)
$$\frac{\partial \overline{u}_i}{\partial t} + \overline{u}_j \frac{\partial \overline{u}_i}{\partial x_j} = -\frac{\partial \overline{p}}{\partial x_i} + \frac{1}{Re} \frac{\partial^2 \overline{u}_i}{\partial x_j \partial x_j} - \frac{\partial \tau_{ij}}{\partial x_j} + F_i$$	(2)
$$\tau_{ij} \approx \overline{u_i' u_j'} \approx \frac{1}{3} \overline{u_k' u_k'} \delta_{ij} - 2\nu_{SGS} \overline{S}_{ij}$$	(3)
$$\nu_{SGS} = C_{MTS} k_{es} T_S$$	(4)
$$T_S^{-1} = \left(\frac{\Delta}{\sqrt{k_{es}}} \right)^{-1} + \left(\frac{C_T}{\left| \overline{S}_{ij} \right|} \right)^{-1}$$	(5)
$$k_{es} = (\overline{u}_k - \hat{\overline{u}}_k)^2$$	(6)
$$\overline{S}_{ij} = \frac{1}{2} \left(\frac{\partial \overline{u}_i}{\partial x_j} + \frac{\partial \overline{u}_j}{\partial x_i} \right)$$	(7)
$$\left| \overline{S} \right| = \left(2 \overline{S}_{ij} \overline{S}_{ij} \right)^{1/2}$$	(8)
$$\Delta = \left(\Delta_x \cdot \Delta_y \cdot \Delta_z \right)^{1/3}$$	(9)
$$C_{MTS} = 0.05$$	(10)
$$C_T = 10.0$$	(11)
$$F_i = -C_{RC} \cdot f\left(y/R, z/R, \right) \cdot \overline{u}_i \cdot V$$, R: Rotor radius	(12)
$$V = \sqrt{\overline{u}^2 + \overline{v}^2 + \overline{w}^2}$$	(13)
$$C_{RC} = 5.0$$	(14)

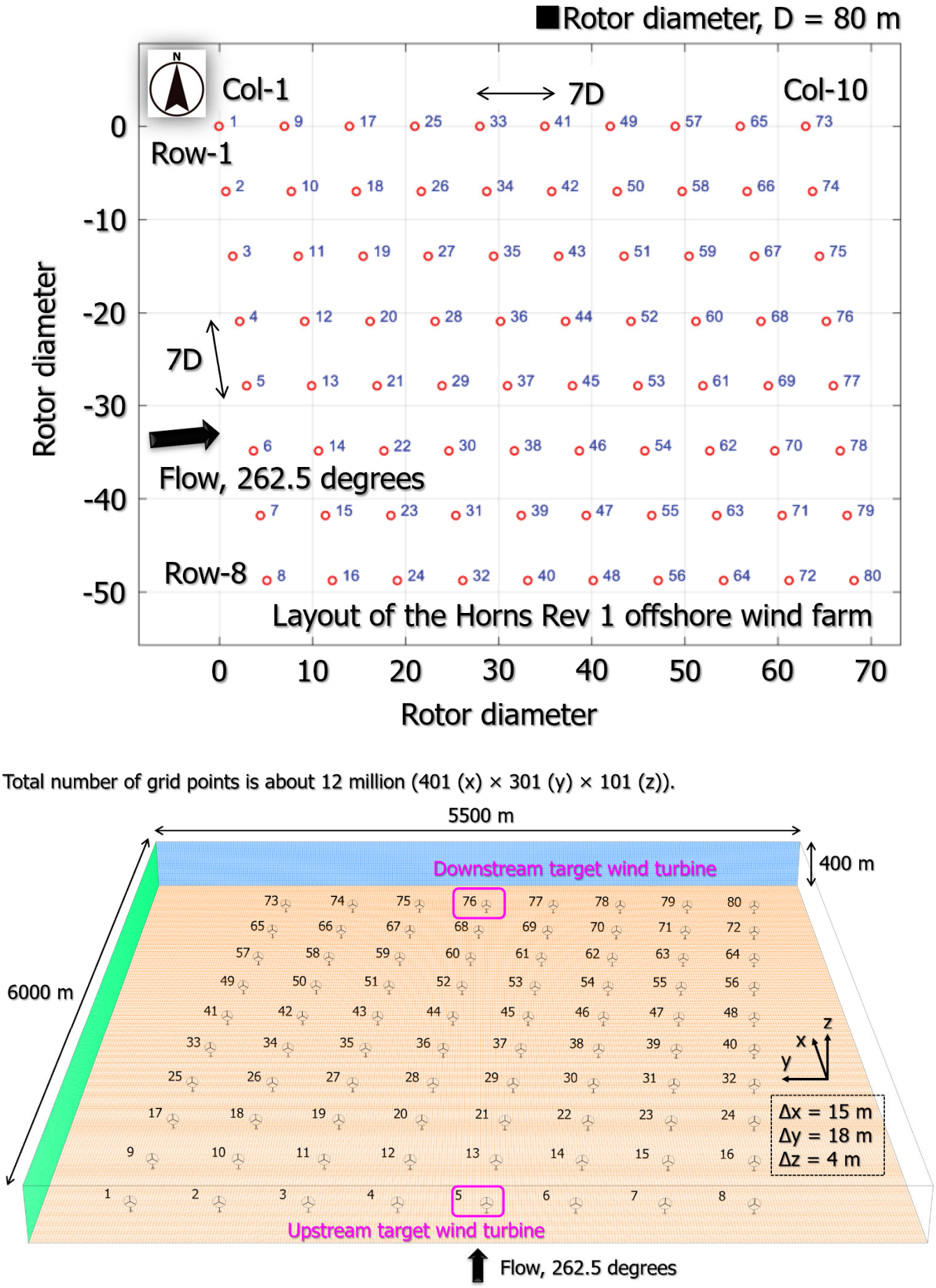

Figure 2. Layout, computational domain, computational grid, and coordinate system for the Horns Rev 1 offshore wind farm.

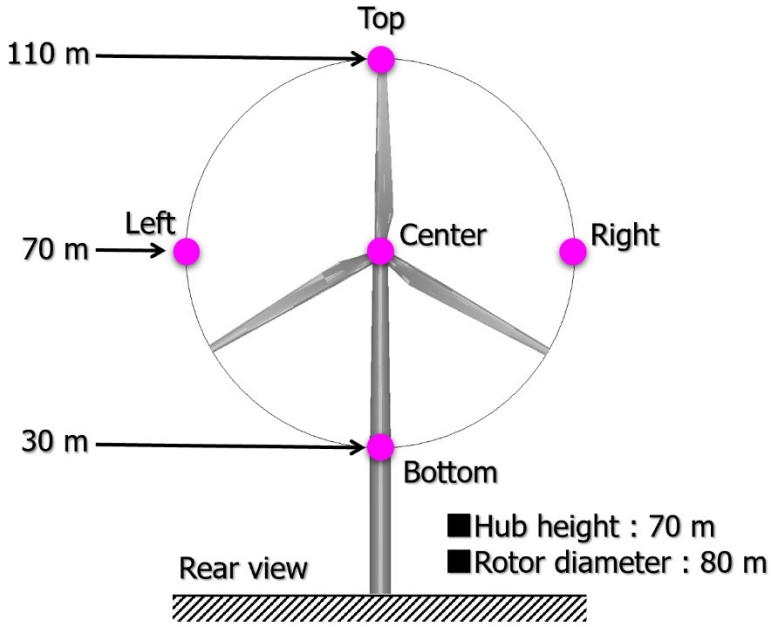

Figure 3. Measurement points in the swept area.

Figure 2 shows a computational domain (6000 m (x) × 5500 m (y) × 400 m (z)), including the total number of grid points and the grid resolutions in the streamwise and cross-stream directions for the Horns Rev 1 offshore wind farm. The wind farm consists of 80 utility-scale wind turbines. The total number of grid points in the computational domain was approximately 12 million (401 (x) × 301 (y) × 101 (z)). In the current simulation, grid resolutions with uniform spacing in all directions were used ($\Delta x = 15$ m, $\Delta y = 18$ m, $\Delta z = 4$ m). As explained earlier, to consider the influence of rotating blades on the flow field, the CFD porous disk wake model (Uchida et al., 2020, 2021) was applied. The influence of the nacelle and tower was ignored. A power law distribution with N = 10 was used as an inlet boundary condition. The lateral and upper boundary conditions were assigned a slip condition, while the outflow section was assigned the Sommerfeld radiation condition (SRC). A no-slip boundary condition was set on the ground. The time step was $\Delta t = 2 \times 10^{-3}$ (R/U_{in}), where U_{in} is the uniform flow speed and R is the radius of the wind turbine blade. To fully develop the flow field in both the near- and far-wake regions downstream of the wind turbine model, time integration from t = 0 to 200 (R/U_{in}) was performed. Flow field statistical processing was performed at t = 100 – 200 (R/U_{in}) in the latter half of the time integration. In this study, five measurement points, as shown in Figure 3, were set to quantitatively evaluate the wind speed entering the swept area of the wind turbine.

Table 1. Main specifications of the GPU workstation used in this study.

CPU	Xeon W-2265 (12 cores @ CPU 3.50 GHz)
Memory	128GB (16 GB DDR4-2933 ECC RDIMM × 8)
SSD	480 GB × 2
GPU	NVIDIA RTX A6000 (48 GB)
OS	CentOS 7.6
• CUDA 11.4 • NVIDIA HPC SDK 21.9 • Intel Parallel Studio XE 2019 update 5	

Table 1 shows the main specifications of the GPU workstation used in this study. In the current study, OpenACC directives were inserted into the Fortran program developed by the first author. Next, the program was compiled by the NVIDIA HPC SDK using the "-acc" option. Finally, the inserted directives were enabled and the executable file for the GPU was generated. LES simulation by a new SX-Aurora TSUBASA vector supercomputer was also performed for comparison with the calculation time of the GPU. In this study, we used a 1VE (vector engine) consisting of eight cores (theoretical peak performance: 2.16 TFLOPS).

3. Numerical Results and Discussion

First, let us consider the comparison of calculation speed ratios, as shown in Figure 4. Based on the calculation time using 12 cores of the Xeon W-2265 (CPU 3.50 GHz) in the same workstation, the GPU calculation time using NVIDIA RTX A6000 increased by approximately 10 times. It was almost the same as the 1VE calculation time of the new SX-Aurora TSUBASA vector supercomputer (eight cores/theoretical peak performance: 2.16 TFLOPS). The latest high-performance GPU used in this study, the NVIDIA RTX A6000, has 48 GB of memory, even with a graphics card. Therefore, despite the lack of extremely large computational resources (massively parallel computing devices), large parallel computations of the wake interaction within large offshore wind farms using tens of millions of grid points are still possible. Further performance improvement is expected, and we do not doubt that high-performance computing for large offshore wind farms using a single GPU will become a reality.

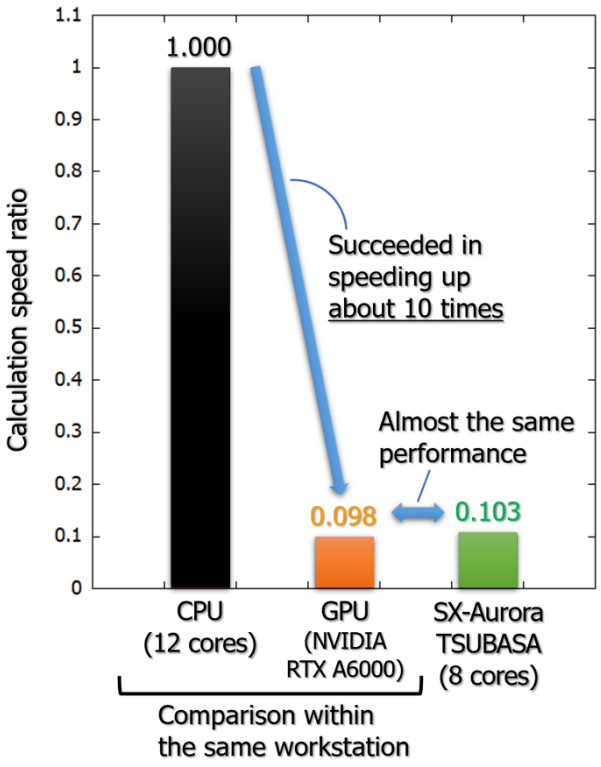

Figure 4. Comparison of calculation speed ratios.

From here on, we discuss the wake flows behind the wind turbines in the wind farm. The most common analytical engineering wake model is the so-called Park wake model (Jensen et al., 1983, 1986). The Park wake model implements a simple formula for the size of the wake deficit and its expansion

downstream with a single adjustable parameter (wake decay constant). Therefore, the Park wake model is still widely used for evaluating business feasibility in the wind industry in Japan and overseas. Figure 5 shows the color shading of non-dimensional scalar horizontal wind speed at the hub height (70 m) by the analytical Jensen wake model. As has already been pointed out, it is extremely difficult to accurately predict the mutual interference between wind turbines using the Park wake model. Figure 6 shows the color shading of non-dimensional time-averaged scalar horizontal wind speed at the hub height by the CFD porous disk wake model. In contrast to the numerical results by the analytical Jensen wake model shown in Figure 5, Figure 6 shows that the mutual wake interferences are well reproduced.

Here, we focus on wind turbines #5 and #76, which were selected as target wind turbines in the present research, shown on the right side of Figure 6. It should be noted that the time-averaged wind speed distributions immediately upstream of wind turbines #5 and #76 are almost the same, as shown in Figure 6. A similar trend can also be confirmed in Figures 5, 7, and 9.

Figure 7 shows the time-averaged vertical wind speed distributions immediately upstream of wind turbines #5 and #76; it can be seen that the wind speeds of both wind turbines are almost the same and the wind velocity is low compared to the inflow profile at the wind turbine hub height (70 m).

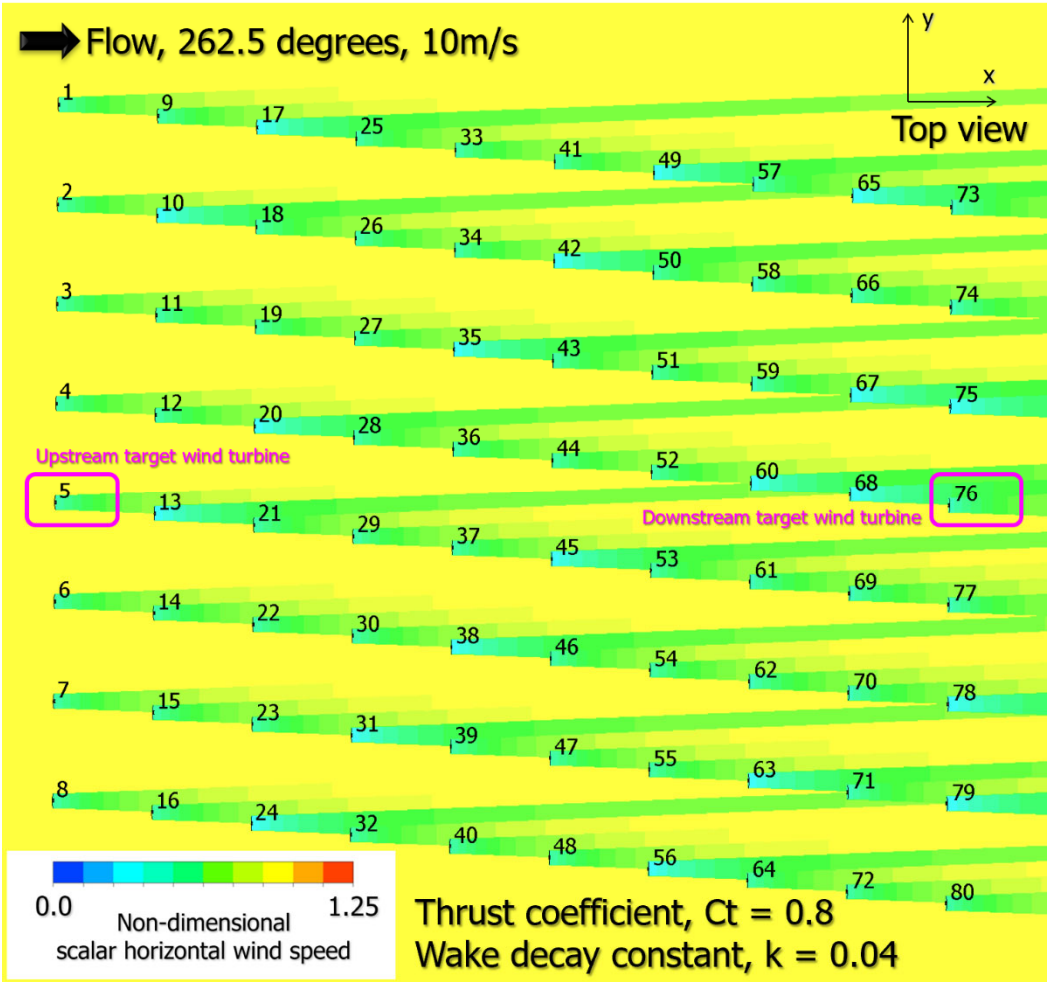

Figure 5. Color shading of non-dimensional scalar horizontal wind speed at the hub height (70 m) by the analytical Jensen wake model.

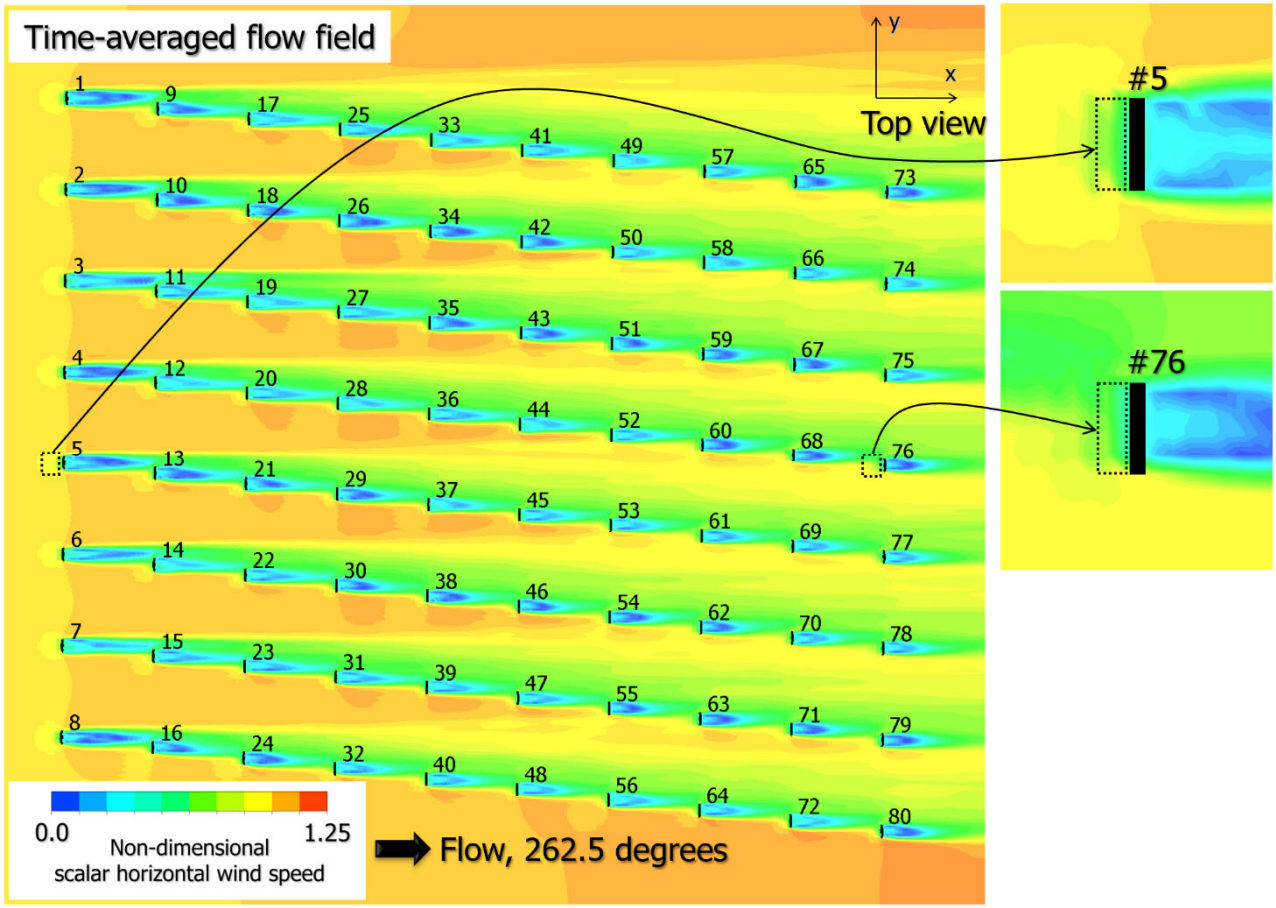

Figure 6. Color shading of non-dimensional time-averaged scalar horizontal wind speed at the hub height by the CFD porous disk wake model.

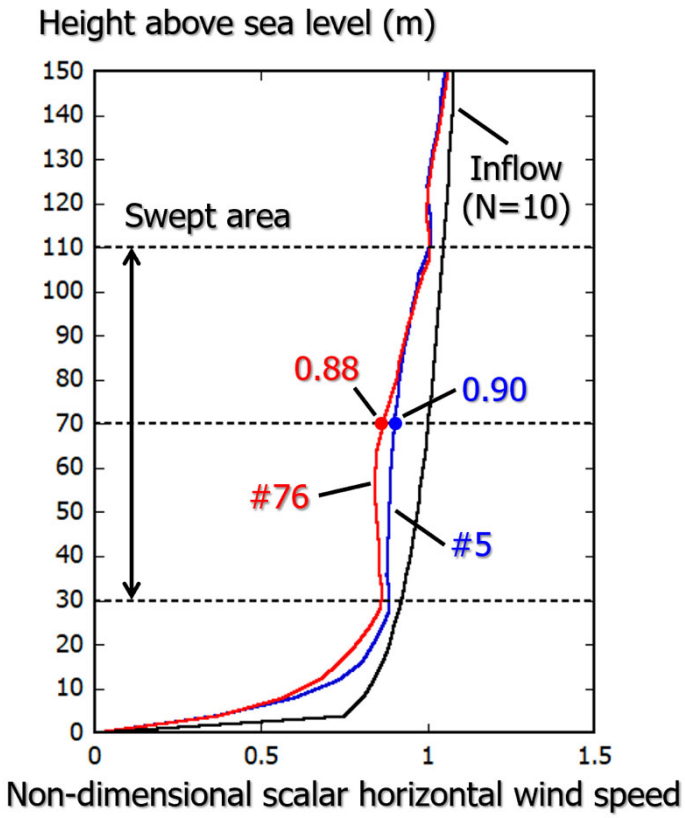

Figure 7. Time-averaged vertical wind speed distributions immediately upstream of wind turbines #5 and #76.

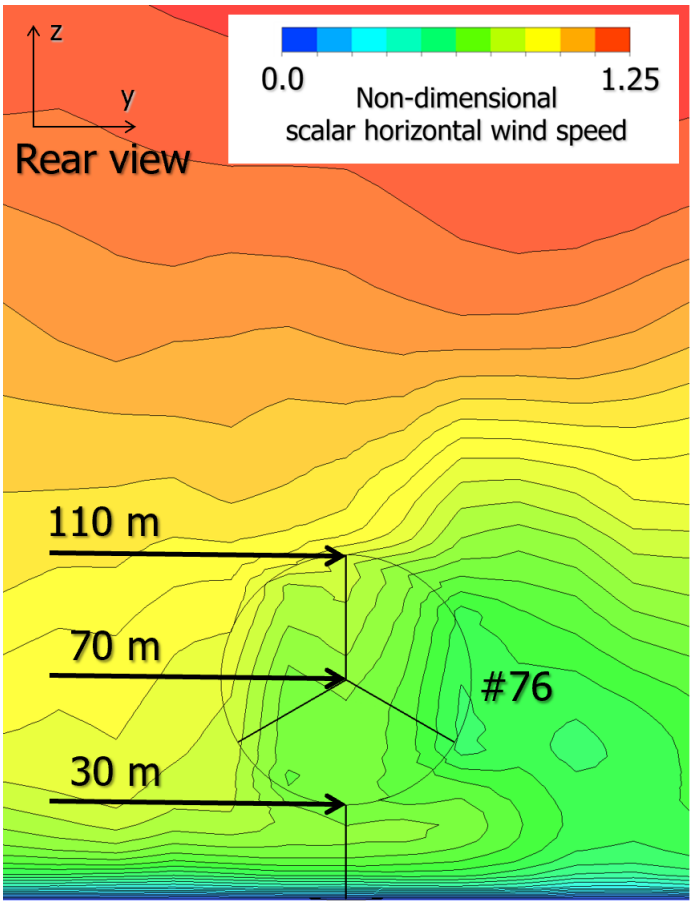

Figure 8. Rearview color shading of the non-dimensional time-averaged scalar horizontal wind speed of wind turbine #76.

Figure 8 shows the rear view color shading of the non-dimensional time-averaged scalar horizontal wind speed in the swept area of wind turbine #76. Focusing on the spatial distribution within the swept area of the wind turbine, we can see that it is extremely complicated. The main cause is presumed to be mutual interferences between wind turbine wakes upstream of wind turbine #76. Furthermore, related to these phenomena, it is thought that unsteady turbulent flow occurs around wind turbine #76.

Now, we consider the reason why there was no significant difference in the non-dimensional time-averaged scalar horizontal wind speeds between wind turbine #5 located on the upstream-most side, and wind turbine #76 located on the downstream-most side. At the same time, we consider the unsteady flow behavior around wind turbine #76 in detail. Figure 9 compares the time histories of the non-dimensional scalar horizontal wind speeds of #5 and #76. These wind speed values were evaluated based on the streamwise and cross-stream velocity components at the hub height (70 m) immediately upstream of wind turbines #5 and #76, as shown in Figure 3. In the figure, the blue line indicates the numerical results of wind turbine #5, and the red line provides the numerical results of wind turbine #76. First, note the time-averaged wind speed shown on the right side of Figure 9. As mentioned earlier, no significant difference appeared between wind turbine #5 located on the upstream-most side, and wind turbine #76 located on the downstream-most side in the current study. As expected, for wind turbine #5, which is located on the upstream-most side, the non-dimensional scalar horizontal wind speed showed an almost constant value, and no temporal fluctuation appeared. However, for wind turbine #76, which is located on the downstream-most side, the waveform of the non-dimensional scalar horizontal wind

speed fluctuated greatly with time. From the time history waveform of wind turbine #76 shown in Figure 9, it was clarified that an unsteady flow occurred around wind turbine #76 due to mutual interferences of wind turbine wakes.

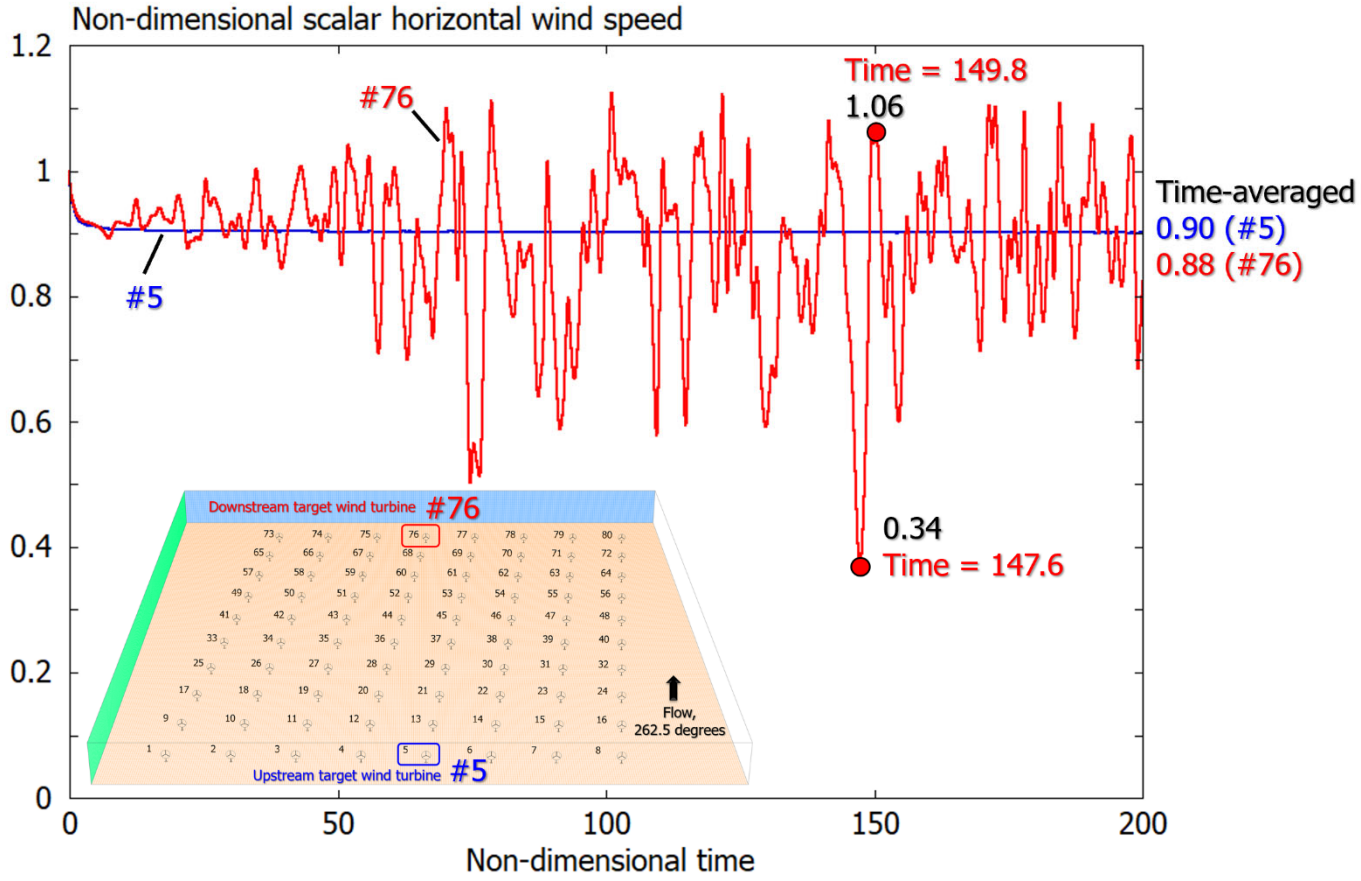

Figure 9. Comparison of the time histories of the non-dimensional scalar horizontal wind speeds of #5 and #76. These wind speed values were evaluated at the hub center shown in Figure 3.

Figure 10 shows the color shading of the non-dimensional instantaneous scalar horizontal wind speed at the time when the scalar horizontal wind speed just upstream of wind turbine #76 was the lowest (non-dimensional time = 147.6). The enlarged view in Figure 10b shows the area surrounded by the black dotted line in Figure 10a. First, in the perspective view shown in Figure 10a, it can be seen that wakes are generated from each wind turbine and that they strongly interfere with one another on the downstream side. In the enlarged view shown in Figure 10b, the relatively large velocity deficit region (surrounded by the black dotted line in Figure 10b) generated from the wind turbine group located on the upstream side can be clearly observed at the position immediately upstream of wind turbine #76.

Figure 11 shows the corresponding flow characteristics of wind turbine #76 at non-dimensional time = 147.6. Figure 11a shows the rear view color shading of the non-dimensional scalar horizontal wind speed. Figure 11b shows the vertical wind speed distributions immediately upstream of wind turbine #76. From these numerical results, it can be clearly observed that in the spatial wind speed distribution in the swept area of , wind turbine #76 is extremely complicated and that there is a significant deficit in wind velocity.

Next, the situation that occurs following Figures 10 and 11 is shown, and these numerical results are considered. Figure 12 shows the color shading of the non-dimensional instantaneous scalar horizontal wind speed

at the time when the scalar horizontal wind speed just upstream of wind turbine #76 was the highest (non-dimensional time = 149.8). It should be noted here that the wind speed just upstream of wind turbine #76 was 1.2 times faster than that of wind turbine #5, which is located on the upstream-most side. Through careful observation of Figure 12, we can see that the local speed-up region generated by the mutual interference of the wind turbine wakes is about to pass through wind turbine #76. In the time history of the non-dimensional scalar horizontal wind speed of wind turbine #76, as shown in Figure 9, although there are many time zones of velocity deficit, the local speed-up phenomenon is confirmed at the same frequency. In other words, the series of numerical results obtained in the current study suggests that the mutual interference phenomenon of wind turbine wakes may bring about a local speed-up region around the wind turbines located on the downstream side of large offshore wind farms.

Figure 13 shows the corresponding flow characteristics of wind turbine #76 at non-dimensional time = 149.8. Figure 13a shows the rear view color shading of the non-dimensional scalar horizontal wind speed. Figure 13b shows the vertical wind speed distributions immediately upstream of wind turbine #76. Similar to the numerical results shown in Figure 11b, the spatial wind speed distribution in the swept area of wind turbine #76 shown in Figure 13a is not uniform and is very complex. In contrast, Figure 13b shows significant wind speed recovery due to enhanced wind turbine wake mixing.

The wind turbines installed in offshore wind farms are getting larger year by year. Therefore, accurately predicting the wind speed distribution in the swept area will undoubtedly become more and more important in the future, as it relates to the prediction of the power output and fatigue life of offshore wind turbines. In addition, the method of selecting a representative wind speed in the swept area has become an extremely important issue. Therefore, we finally discuss the process of selecting measurement points in the swept area shown in Figure 3. Figure 14 shows a comparison of the time histories of the non-dimensional scalar horizontal wind speeds of wind turbine #76. The solid red line indicates the numerical results based on the horizontal wind speed only at the hub center (the same as the numerical results shown in Figure 9), and the solid black line represents the average value of the horizontal wind speeds at the five points in the swept area. As expected, it is clear that the behaviors of both changed over time and showed similar tendencies. The numerical results, when considering more wind speed information, have a smaller fluctuation amplitude than the numerical results using only one point of wind speed information. As a result, the numerical results, when considering more wind speed information, have a larger average value than the numerical results when using only one point. Considering the above, we suggest that in the case of a wind turbine with a larger swept area, more wind speed information should be used to evaluate the representative wind speed in the swept area.

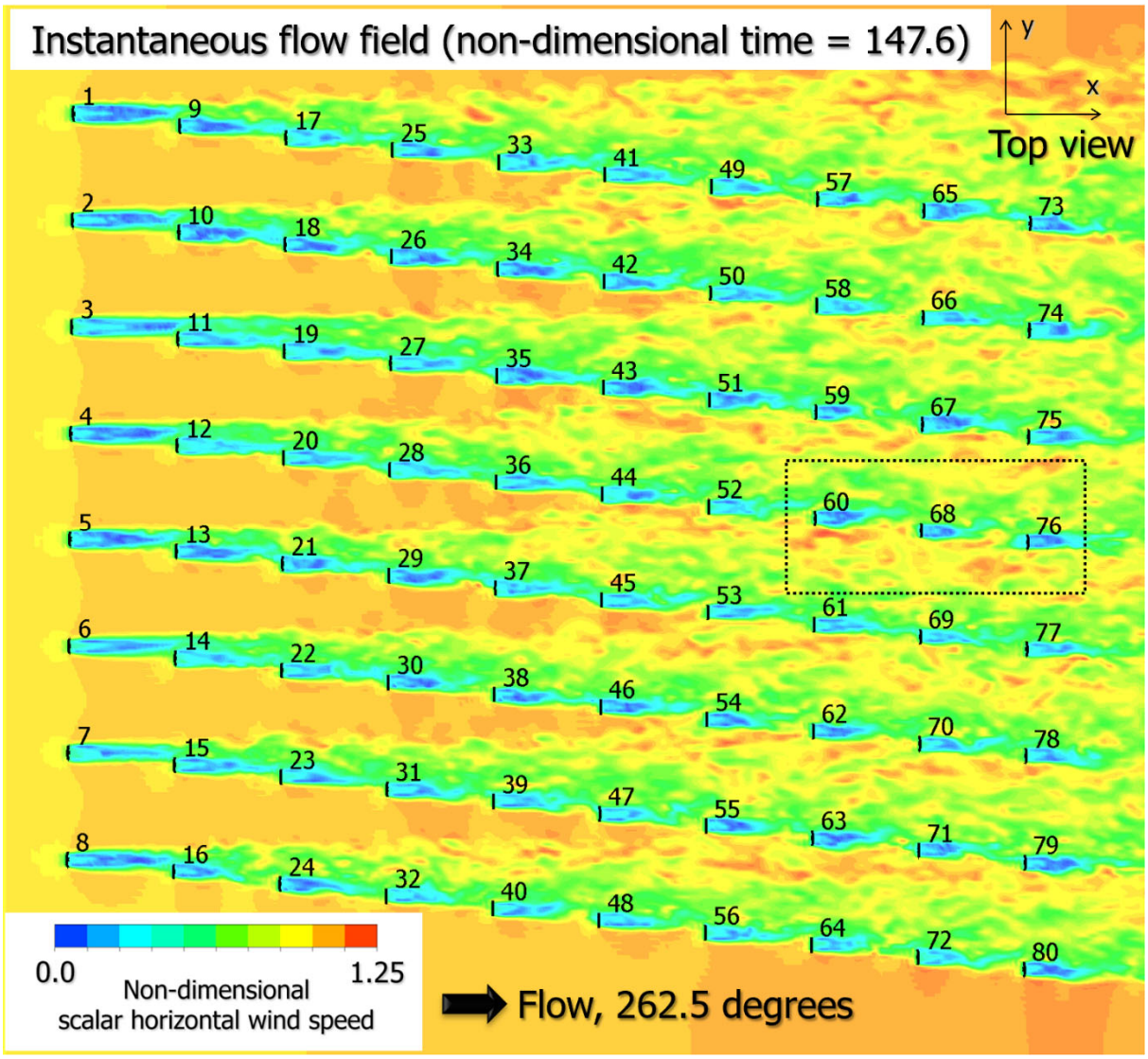

(a)

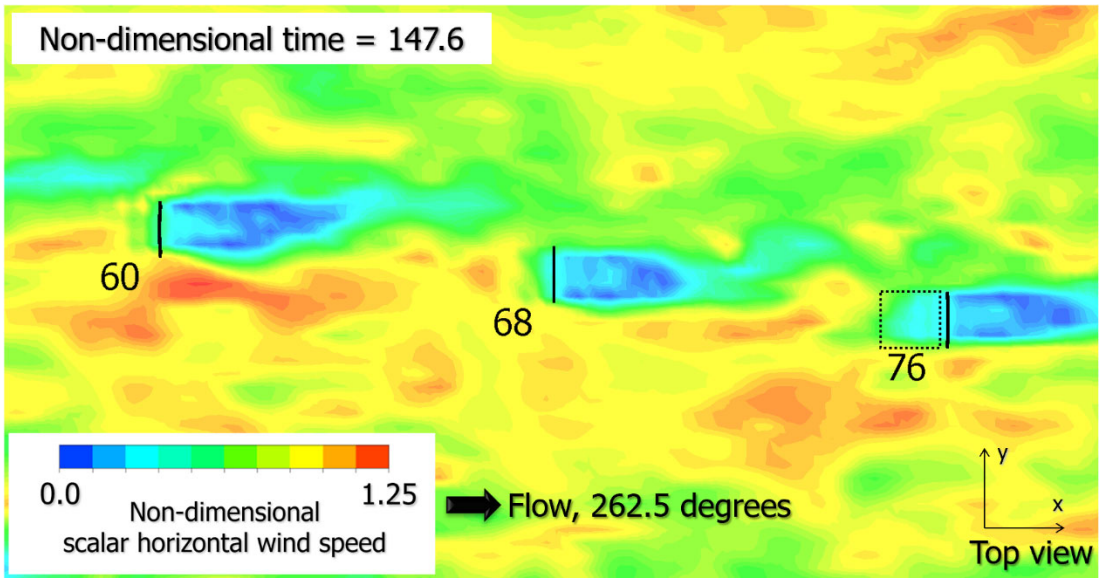

(b)

Figure 10. Color shading of the non-dimensional instantaneous scalar horizontal wind speed at the time when the scalar horizontal wind speed just upstream of wind turbine #76 was the lowest (non-dimensional time = 147.6): (a) Perspective view and (b) enlarged view.

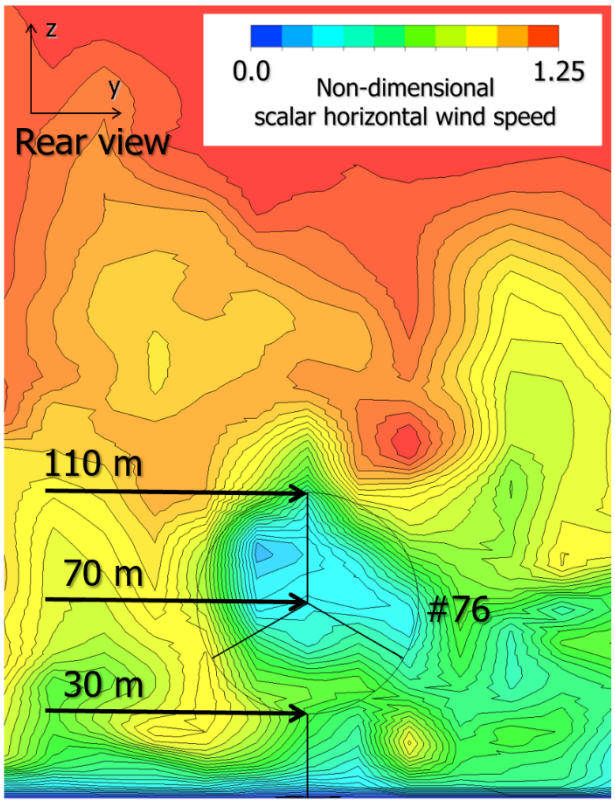

(a)

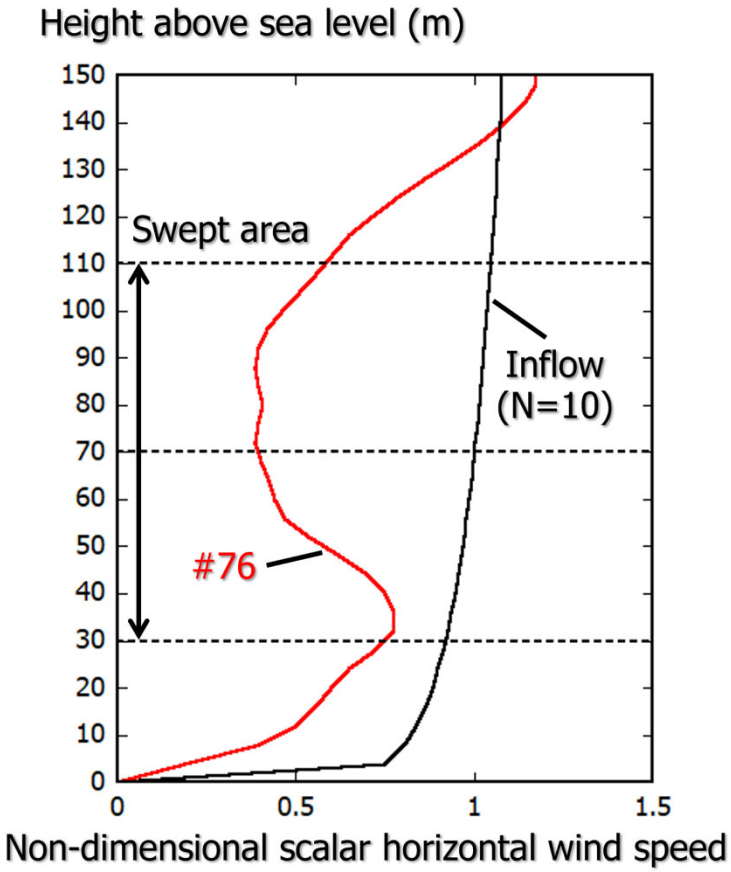

(b)

Figure 11. Flow characteristics of wind turbine #76 at non-dimensional time = 147.6: (a) Rear view color shading of the non-dimensional scalar horizontal wind speed and (b) vertical wind speed distributions immediately upstream of wind turbine #76.

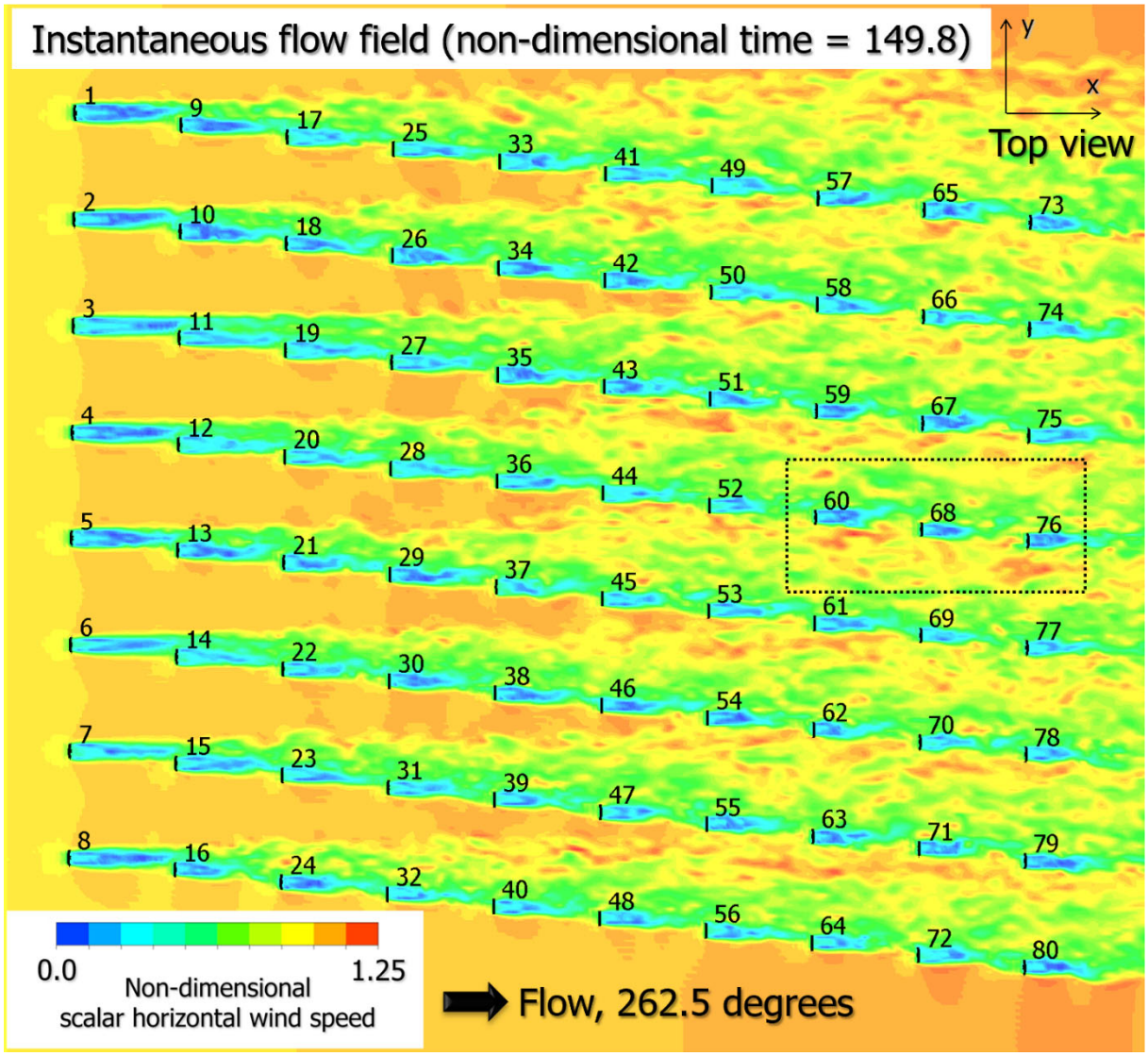

(a)

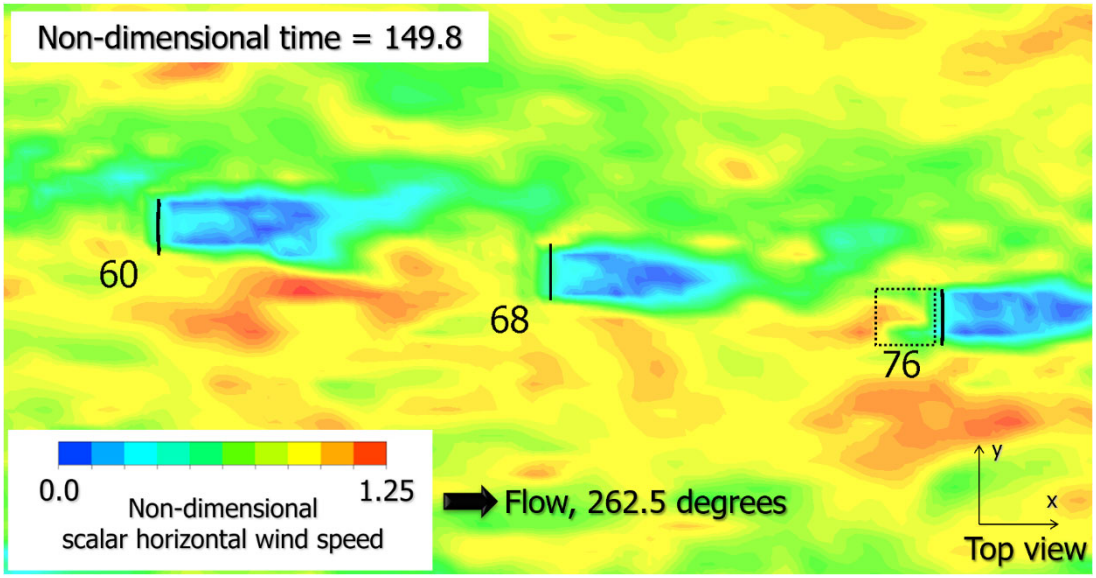

(b)

Figure 12. Color shading of the non-dimensional instantaneous scalar horizontal wind speed at the time when the scalar horizontal wind speed just upstream of wind turbine #76 was the highest (non-dimensional time = 149.8): (a) Perspective view and (b) enlarged view.

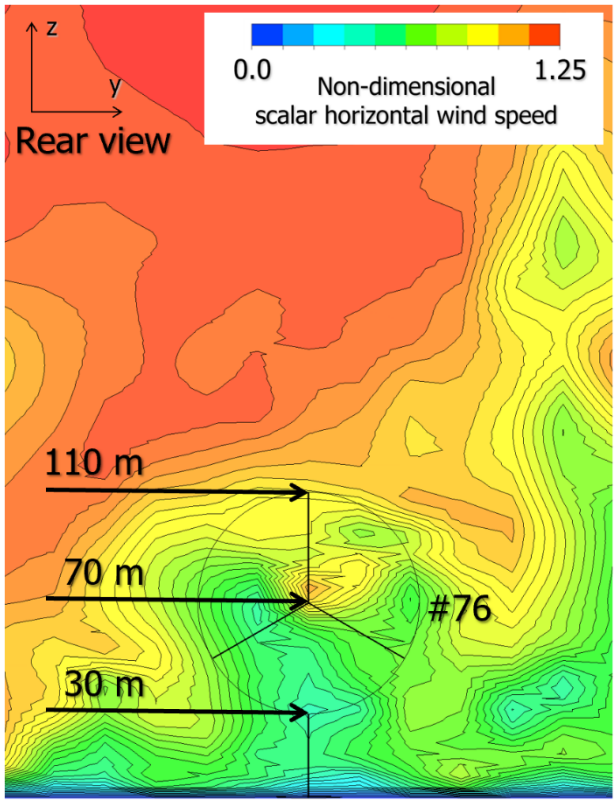

(a)

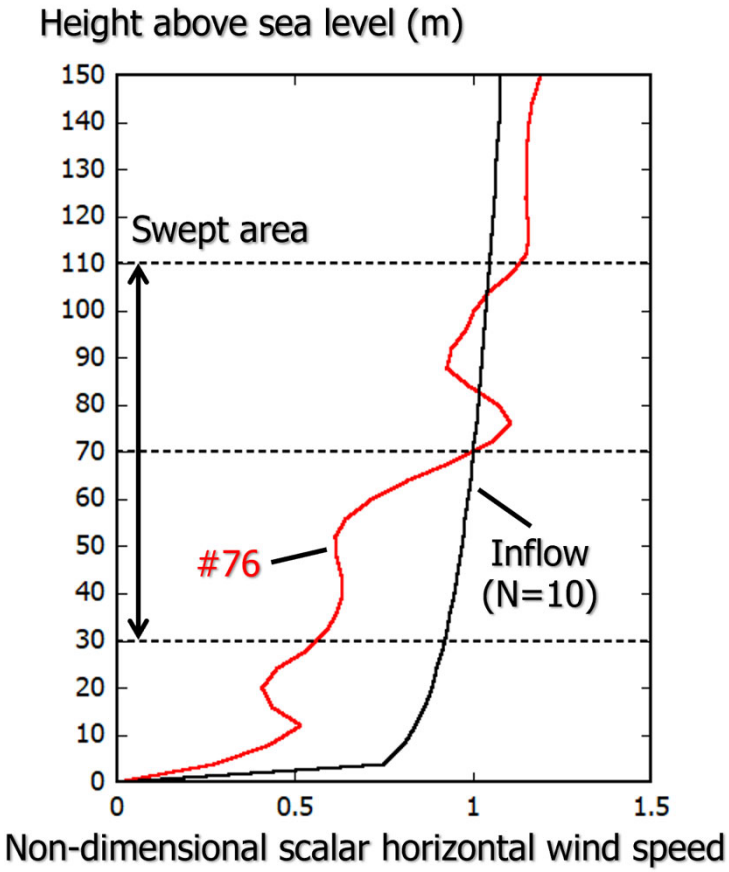

(b)

Figure 13. Flow characteristics of wind turbine #76 at non-dimensional time = 149.8: (a) Rear view of color shading of the non-dimensional scalar horizontal wind speed and (b) vertical wind speed distributions immediately upstream of wind turbine #76.

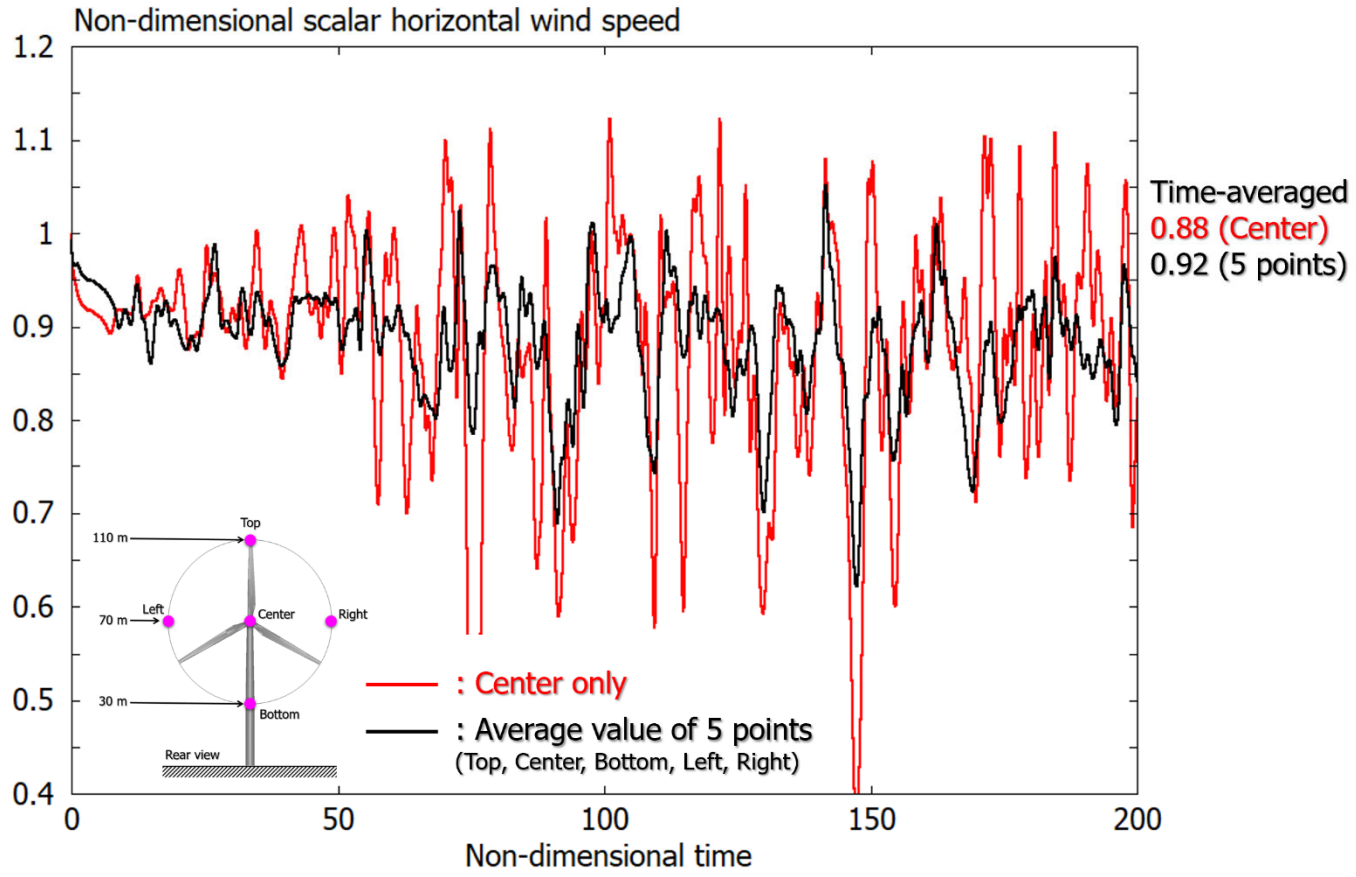

Figure 14. Comparison of the time history of the non-dimensional scalar horizontal wind speed of wind turbine #76. The solid red line indicates the numerical results based on the horizontal wind speed only at the hub center (the same as the numerical result shown in Figure 5), and the solid black line represents the average value of the horizontal wind speeds at the five points in the swept area.

4. Conclusions

In this work, GPU computation using NVIDIA RTX A6000 succeeded in achieving an approximately 10 times faster speed than CPU computation using 12 cores of Xeon W-2265 (CPU 3.50 GHz). This almost matched the 1VE calculation time of the new SX-Aurora TSUBASA vector supercomputer (eight cores/theoretical peak performance: 2.16 TFLOPS). Looking ahead, we expect to see further performance improvements and predict that high-performance computing for large offshore wind farms using a single GPU will become a powerful tool.

Next, careful consideration of the flow fields obtained in the current LES study clarified that an unsteady turbulent flow occurred around wind turbine #76 due to mutual interferences of wind turbine wakes. Furthermore, the mutual interference phenomenon of wind turbine wakes may generate a local speed-up region around wind turbine #76, located on the downstream side of large offshore wind farms. We expect that further research will lead us to establish a more efficient wake steering method (Houck, 2021).

The wind turbines installed in offshore wind farms are getting larger year by year. Therefore, accurately predicting the wind speed distribution in the swept area will undoubtedly become more and more important in the future, as it relates to the prediction of the power output and fatigue life of offshore wind turbines. In addition, the method of selecting a representative wind speed in the swept area has become an extremely important issue.

Therefore, we finally discussed the process of selecting measurement points in the sweep. As a result, we suggest using more wind speed information to evaluate the representative wind speed in the swept area.

Acknowledgments

Part of this work was supported by joint research with Eurus Energy Holdings Corporation and the Adaptable and Seamless Technology Transfer Program through Target-Driven R&D (A-STEP) from Japan's Science and Technology Agency (JST), grant number JPMJTR211C.

References

Gargallo-Peiró, Abel; Avila, Matias; Owen, Herbert; Prieto-Godino, Luis; Folch, Arnau: Mesh generation, sizing and convergence for onshore and offshore wind farm Atmospheric Boundary Layer flow simulation with actuator discs, Journal of Computational Physics, volume 375, pages 209-227, 2018. https://doi.org/10.1016/j.jcp.2018.08.031

Hasager, C.B.; Nygaard, N.G.; Volker, P.J.H.; Karagali, I.; Andersen, S.J.; Badger, J. Wind Farm Wake: The 2016 Horns Rev Photo Case. Energies 2017, 10, 317. https://doi.org/10.3390/en10030317

Houck, Daniel R., 2021. Review of wake management techniques for wind turbines. doi:10.1002/we.2668.

Inagaki, M., Kondoh, T., and Nagano, Y.,: A mixed-time-scale SGS model with fixed model-parameters for practical LES. ASME. J Fluids Eng January 127(1), 1–13, 2005. https://doi.org/10.1115/1.1852479

Jensen, N.O. A Note on Wind Generator Interaction; Technical Report Risoe-M-2411(EN); Risø National Laboratory: Roskilde, Denmark, 1983.

Katic, I., Højstrup, J., Jensen, N. O. A simple model for cluster efficiency. In Proceedings of the European Wind Energy Association Conference & Exhibition (EWEC'86). 1, 407-410, 1987.

Kajishima, T. Upstream-shifted interpolation method for numerical simulation of incompressible flows. Bull. Jpn. Soc. Mech. Eng. B, 60, 3319, 1994.

Kawamura, T.; Takami, H.; Kuwahara, K. Computation of high Reynolds number flow around a circular cylinder with surface roughness. Fluid Dyn. Res., 1, 145-162, 1986.

Kenji ONO and Takanori UCHIDA, High-Performance Parallel Simulation of Airflow for Complex Terrain Surface, Modelling and Simulation in Engineering, Volume 2019, Article ID 5231839, 2019. https://doi.org/10.1155/2019/5231839

Kim, J.; Moin, P. Application of a fractional-step method to incompressible Navier-Stokes equations. J. Comput. Phys., 59, 308, 1985.

Porté-Agel, F., Bastankhah, M., Shamsoddin, S.: Wind turbine and wind-farm flows: a review. Boundary-Layer Meteorol 174, 1–59, 2020.

Uchida, T., Li Graham., Comparison of RANS and LES in the prediction of airflow field over steep complex terrain. Open J Fluid Din 8, 286-307, 2018.

Takanori UCHIDA, Yoshihiro TANIYAMA, Yuki FUKATANI, Michiko NAKANO, Zhiren BAI, Tadasuke YOSHIDA and Masaki INUI, A New Wind Turbine CFD Modeling Method Based on a Porous Disk Approach for Practical Wind Farm Design, Energies, 13(12), 3197, 2020. https://doi.org/10.3390/en13123197

Takanori Uchida,Tadasuke Yoshida,Masaki Inui and Yoshihiro Taniyama, Doppler Lidar Investigations of Wind Turbine Near-Wakes and LES Modeling with New Porous Disc Approach, Energies 2021, 14(8), 2101. DOI:https://doi.org/10.3390/en14082101